JOURNAL OF MATERIALS SCIENCE 14 (1979) 2001–2012

Residual stress effects in sharp contact cracking

Part 1 *Indentation fracture mechanics*

D. B. MARSHALL, B. R. LAWN
Department of Applied Physics, School of Physics, University of New South Wales, N.S.W. 2033, Australia

A study is made of residual stress effects in the mechanics of median fracture in sharp indenter contact. Starting with a simplistic treatment of the elastic–plastic indentation field, the problem is conveniently resolved into two separable parts, involving reversible (elastic) and irreversible (residual) components. The assumption of geometrical similarity in the residual field about the deformation zone, later backed up by stress birefringence measurements, leads to a stress intensity factor for median crack propagation containing the elastic and residual parts as the sum of two terms. The resulting formulation for equilibrium fracture shows some differences in the crack response during the loading and unloading half-cycles. By imposing certain stress states on the specimen surface during indentation the residual component of the field may actually cause the median crack to continue in downward extension as the indenter is withdrawn, a response which is especially amenable to experimental investigation. Direct observations of median crack evolution in soda-lime glass confirm this and other essential predictions of the fracture mechanics theory. The contribution of the residual component to the crack growth is found to be by no means secondary in importance to that of the elastic component.

1. Introduction

Indentation fracture techniques are proving to be useful in the characterization of brittle surfaces [1]. A well-controlled contact test offers the prospect of highly reproducible deformation–fracture geometry, together with simplicity and economy in data accumulation. It is now established that there are two basic types of indentation fracture pattern, depending on whether the contact is essentially elastic ("blunt" indenters) or plastic ("sharp" indenters) [1, 2]. Of these, the sharp indenter configuration is the more severe, and is therefore especially pertinent to engineering properties such as strength, wear and erosion.

The true nature of the stress field about a sharp indenter contact is, of course, elastic–plastic [2]. Within this field a system of penny-like cracks evolves once some threshold is reached in the loading, namely "median" (or "radial") cracks, on symmetry planes containing the load axis and principal impression diagonals, and "lateral" cracks, on a saucer-shaped surface centred near the impression base. The first attempts at a fracture mechanics analysis of the sharp indenter system [3, 4] focussed on the median cracks, noting that in soda-lime glass these cracks formed primarily during indenter *loading*, and were presumably being driven predominantly by elastic components of the field. Lateral cracks, on the other hand, formed entirely during *unloading*, indicating a driving force in association with residual stresses about the irreversible deformation zone. Thus whilst the fully propagating median crack could be treated to a first approximation in terms of a centre-loaded half-penny configuration [4], analysis of lateral crack development appears to require a more detailed solution to a complex elastic–plastic stress problem. Consequently, properties more closely allied to median rather than lateral crack generation have proved simpler to model in terms of indentation fracture mechanics. The relatively sound position of present-day

0022–2461/79/082001–12 $03.20/0 © *1979 Chapman and Hall Ltd.*

theories of strength degradation as compared to surface erosion in particle contact situations is a notable manifestation of this state of affairs [2].

Although the basic form of the fracture mechanics relations for centre-loaded penny-like cracks appears to be well satisfied by the median flaws, there is a growing body of evidence that even in this case residual stress effects are far from insignificant. Direct observation of the fracture evolution during one complete indentation cycle in glass shows that the ultimate radial symmetry of the medians is not achieved uniformly: whereas the bulk of the downward extension into the material does indeed occur on loading, a considerable amount of the sideways extension at the surface occurs as the indenter is being withdrawn [4]. Also, where sharp indenters are used to produce a dominant starting flaw for controlled strength testing, critical stress intensity factors evaluated from measurements of the crack size tend to be somewhat less than those determined by more conventional means (e.g. double cantilever or double torsion specimens), typically by $\approx 30\%$ [5, 6]. Such evidence is indicative of a residual opening force on the indentation cracks, consistent with the fact well known to glaziers that secondary fractures induced by a scribing tool continue to grow long after the cutting operation has been completed. Petrovic *et al.* [5] demonstrated the central role of the plastic deformation zone about the hardness impression as a source of the residual stress field: In a series of tests on ceramic specimens in which the surfaces were either progressively polished or annealed, a strength recovery commensurate with the true critical stress intensity factor was observed.

Our aim in this study is to quantify the residual stress effect in sharp indenter deformation–fracture mechanics, and to investigate the implications of these effects in the modelling of contact related properties for brittle solids. The potential importance of the phenomenon to be discussed in some depth here has already been demonstrated in a preliminary report published elsewhere [7]. In Part 1 of the study a fracture mechanics framework is established for describing the evolution of median fracture under various indentation loading conditions. Vickers indentation tests on soda-lime glass provide a convenient model system for experimental analysis. Part 2 will concern itself with the incorporation of residual stress terms in strength degradation analysis.

2. Fracture mechanics relations for median cracks in an elastic–plastic field

2.1. Stress intensity factors

A complete description of fracture evolution within an elastic–plastic indentation field would begin with a detailed analysis of stress distributions along the prospective crack paths [8]. Such an analysis poses formidable obstacles, however, with the need to accommodate nonlinear constitutive relations for the material under consideration, appropriate boundary conditions at the indenter–specimen interface, and the presence of free surface outside the contact area (improperly neglected in commonly adopted "expanding cavity" models). Recent attempts at stress computations along these lines serve to highlight both the extreme complexity and the sensitivity to starting assumptions inherent in the general indentation field [9, 10]. It is accordingly in the interest of providing insight without complication that we adopt a somewhat phenomenological approach to the question of residual stress effects in this work, resorting to detailed stress field considerations only where it is necessary to account for certain anomalous features in the crack patterns.

For this purpose we consider the field which drives the indentation cracks to consist of well-defined, separable components, and make use of the property of linear superposition of *stress intensity factors* [8] to determine the net mechanical force on the fracture system. Suppose first the field arises solely from an indentation load P, as in Fig. 1a. Then the stress tensor at any point in the indented solid may be written as σ_{ep}, denoting an elastic–plastic quantity. Upon removal of the load, Fig. 1b, a component σ_r persists at the point under consideration. Now in the event that a negligible amount of reversed plasticity occurs during the unloading half-cycle, it is clear that *re*loading the indenter to P will restore the configuration of Fig. 1a, and in so doing will contribute a purely elastic stress component σ_e to the field [11]. That is, the elastic–plastic stress field of a fully loaded indenter may be considered as the superposition of the residual field in the unloaded solid and the field of an ideally elastic contact:

$$\sigma_{ep} = \sigma_e + \sigma_r. \tag{1}$$

In this approximation the requirements for a fracture mechanics solution to the basic median

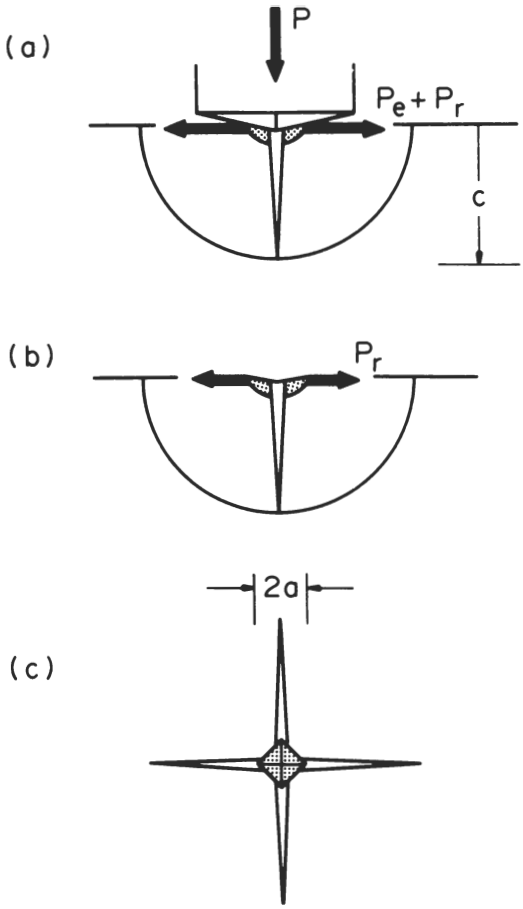

Figure 1 Median crack configuration, idealised here for Vickers indentation geometry. Side views: (a) normal indenter load P generates median opening forces P_e (elastic field component) and P_r (residual field component); (b) load removal eliminates only the P_e component. Lateral cracks (not shown) generate during stage (b). Surface view (c) depicts classical radial crack pattern. Surface stresses (not shown) may also drive the cracks.

crack problem reduce to finding appropriate expressions for the corresponding stress intensity factors K_e and K_r.

The case of a perfectly elastic indentation field has been dealt with in full elsewhere [4]. For the fully propagating median crack of ideal half penny geometry (Fig. 1), radius c, it is readily shown that $K_e \propto P_e/c^{3/2}$, where P_e is the effective wedge opening component of force delivered by the indenter at the crack centre. Geometrical considerations verify that $P_e \propto P$, so

$$K_e = \chi_e P/c^{3/2}, \tag{2}$$

with the dimensionless indenter/specimen constant χ_e some function of indenter angles, contact friction, and free surface effects.

An analogous formulation may be derived for the residual stress intensity factor. We assume that incompatibility of reversible and irreversible regions beneath the unloading indenter generates an effective wedge opening force P_r at the deformation zone (Fig. 1) [6]. This force scales with the intensity of the residual stress field and the cross-sectional area of the deformation zone over which it acts; or, residual stress intensity $\propto P_r/a^2$, where a is a characteristic linear dimension of the hardness impression. For indentations which show geometrical similarity with load, the residual stress must also be expected to scale with the hardness, i.e. residual stress intensity $\propto H \propto P/a^2$ (mean indentation pressure). Thus we conclude $P_r \propto P$. If we now write $K_r \propto P_r/c^{3/2}$ $(a \ll c)$ corresponding to penny-like cracks with constant force loading at their centres, we obtain

$$K_r = \chi_r P/c^{3/2}, \tag{3}$$

where χ_r is another dimensionless indenter–specimen constant.

The similarity of Equations 2 and 3 enables us to write down a single expression of the form $\chi P/c^{3/2}$ for the stress intensity factor corresponding to median crack propagation at full loading, with $\chi = \chi_e + \chi_r$. This is the form which has been used without qualification in earlier strength degradation studies. The fact that χ has been shown experimentally to be invariable with load or crack size for specific indentation systems [4] would appear to provide sufficient justification for assuming χ_e and χ_r to be similarly constant. The important distinction to be made here is that the residual term will continue to operate on completion of the indentation process, and must therefore contribute to the stress intensity factor in a subsequent strength test. Part 2 investigates the full implications of this point. Meanwhile, we shall simply note that a detailed fracture mechanics analysis of the median crack system requires both χ_e and χ_r to be specified; and, in view of the assumptions implicit in the derivations of Equations 2 and 3, that these terms are most properly to be regarded as adjustable parameters to be determined empirically for any given indenter–specimen system.

Agents other than the indentation load may contribute to the driving force for median fracture. One example which we shall be considering later in this study is that of a surface stress σ_s acting uniformly over the crack area. The appro-

priate stress intensity factor takes the form [8]

$$K_s = \sigma_s(\pi\Omega c)^{1/2}, \tag{4}$$

where Ω is a dimensionless crack geometry term. There are two ways of special interest here in which such a stress may arise: (1) as a residual surface compression σ_R via a tempering process, such that

$$\sigma_s = -\sigma_R \tag{5a}$$

remains constant throughout subsequent indentation; (2) as a flexural compression during indentation of a non-rigidly supported plate, whence the stress scales with load according to

$$\sigma_s = -\sigma_F^* P/P^*, \tag{5b}$$

σ_F^* being the maximum compression attained at the maximum load P^*.

2.2. Equilibrium crack relations

Let us now investigate the growth evolution of median cracks under equilibrium conditions. Such conditions may be expressed simply by the relation $K = K_c$, where K is the net stress intensity factor and K_c is a critical value identifiable with material "toughness". For the general case where both indentation load and surface stress operate the equilibrium condition becomes

$$K = K_e + K_r + K_s = K_c. \tag{6}$$

Because of the intrinsic irreversibility in the elastic–plastic indentation field we might expect significant differences in the equilibrium fracture configurations at the same load point during the positive and negative half-cycles of the contact sequence. Accordingly, using Equations 2 to 4 to write Equation 6 in expanded form, we consider the loading and unloading relations separately:

$$\chi_e P/c^{3/2} + \chi_r P/c^{3/2} + \sigma_s(\pi\Omega c)^{1/2} = K_c \quad (P\uparrow) \tag{7a}$$

$$\chi_e P/c^{3/2} + \chi_r P^*/c^{3/2} + \sigma_s(\pi\Omega c)^{1/2} = K_c \quad (P\downarrow) \tag{7b}$$

The irreversibility of the residual term once the maximum load P^* is attained is noted in Equation 7b.

Let us now investigate the crack response as a function of indentation load in Equation 7 for each of three surface states, adopting an asterisk/dagger notation to distinguish between maximum load/complete unload equilibrium configurations:

2.2.1. Stress-free surfaces

We take $\sigma_s = 0$, and differentiate Equation 7a to obtain

$$\delta c/\delta P = 2(\chi_e + \chi_r)/3K_c c^{1/2} \quad (P\uparrow)$$

for the loading half-cycle. Thus $\delta c > 0$ for all $\delta P > 0$, i.e. the crack size increases monotonically with load. At maximum loading, $P = P^*$, the corresponding crack size is

$$c^* = [(\chi_e + \chi_r)P^*/K_c]^{2/3}. \tag{8}$$

Similarly, differentiation of Equation 7b gives

$$\delta c/\delta P = 2\chi_e/3K_c c^{1/2} \quad (P\downarrow)$$

for the unloading half-cycle. Again, $\delta c < 0$ for all $\delta P < 0$, i.e. in order to maintain equilibrium the crack must contract monotonically with decreasing load. At complete unloading, $P = 0$, the final equilibrium crack size is

$$c^\dagger = (\chi_r P^*/K_c)^{2/3}. \tag{9}$$

Dividing Equation 9 into Equation 8 then gives

$$c^*/c^\dagger = (1 + \chi_e/\chi_r)^{2/3}, \tag{10}$$

so that, if it were possible to establish an ideal equilibrium crack cycle, one could determine the relative values of χ_e and χ_r from straightforward crack measurements.

2.2.2. Tempered surfaces

Inserting Equation 5a into 7, and differentiating, we get

$$\delta c/\delta P = 2(\chi_e + \chi_r)/[3K_c c^{1/2} + 4\sigma_R(\pi\Omega)^{1/2}c] \quad (P\uparrow)$$

$$\delta c/\delta P = 2\chi_e/[3K_c c^{1/2} + 4\sigma_R(\pi\Omega)^{1/2}c] \quad (P\downarrow)$$

Thus we find that, as for stress-free surfaces, the cracks are predicted to extend monotonically on loading, and likewise to contract on unloading, although at diminishing rates as σ_R is increased. Equation 7 does not give explicit functions of crack size at maximum loading or complete unloading in this case.

2.2.3. Flexed surfaces

With Equation 5b inserted into Equation 7a, differentiation gives

$$\delta c/\delta P = \frac{2[\chi_e + \chi_r - \sigma_F^*(\pi\Omega)^{1/2}c^2/P^*]}{[3K_c c^{1/2} + 4\sigma_F^*(\pi\Omega)^{1/2}cP/P^*]} \quad (P\uparrow).$$

The crack initially expands at a fast rate, $\delta c \sim c^{-1/2}$, but begins to saturate, $\delta c \to 0$, at

$$c^{\infty} = [(\chi_e + \chi_r)P^*/\sigma_F^*(\pi\Omega)^{1/2}]^{1/2} \quad (11)$$

as the load increases indefinitely. Equation 7a does not provide an explicit function of crack size at maximum loading, but c^{∞} serves usefully as an upper bound. Proceeding similarly with Equation 7b gives

$$\delta c/\delta P = \frac{2[\chi_e - \sigma_F^*(\pi\Omega)^{1/2}c^2/P^*]}{[3K_c c^{1/2} + 4\sigma_F^*(\pi\Omega)^{1/2}cP/P^*]} \quad (P\downarrow).$$

With this case the interesting possibility of a response $\delta c > 0$ for $\delta P < 0$ arises. To quantify this, we note that Equation 7b produces the same crack size function at $P = 0$ as for stress free surfaces,

$$c^{\dagger} = (\chi_r P^*/K_c)^{2/3}; \quad (9)$$

i.e. the ultimate equilibrium crack configuration is independent of any reversible flexural loading, even if the intermediate configurations are not. Then the condition $\delta c/\delta P = 0$ at $c = c^{\dagger}$ determines a critical flexural compression level above which the final configuration is attained via crack extension rather than contraction:

$$(\sigma_F^*)_c = \chi_e K_c^{4/3}/\chi_r^{4/3}(\pi\Omega)^{1/2}P^{*1/3}. \quad (12)$$

Note the reduction in $(\sigma_F^*)_c$ as the residual stress term χ_r increases relative to χ_e.

Our calculations in this subsection are conditional on a state of mechanical equilibrium existing throughout the entire indentation cycle. Even in cases where cracks are found to *extend* in an equilibrium manner, however, fracture environments are generally such that the same cracks are unable to *contract* spontaneously; a variety of mechanical and chemical agents act to restrain closure and healing at the fracture interface [8]. This general irreversibility in crack growth needs to be considered when applying the equations derived above. For instance, we have already pointed out the potential usefulness of Equation 10 in evaluating relative values of χ_e and χ_r. This equation involves the final crack size $c^{\dagger}$, via Equation 9; in a proper experimental determination we should ensure that this ultimate unloading configuration is approached in accordance with the condition $\delta c > 0$. The ideal experimental arrangement would therefore appear to be one in which c^* is determined on a stress-free surface, and $c^{\dagger}$ on a suitably flexed surface. We shall see in the following section that this combination of surface stress states may be realized quite simply in a single indentation set-up.

3. Fracture mechanics experiments

3.1. Residual indentation stress field

Our first experiments were aimed at testing the validity of the basic assumptions underlying Equation 3, in particular the geometrical similarity of the residual indentation field. This was done using a standard optical birefringence technique, with a variable compensator attachment on a polarising microscope. Viewed in the crossed-polars setting, the field could be assessed along any prescribed optical path via a measurement of the retardation [12];

$$\Gamma = A \int_0^t \Delta\sigma(z)\, dz, \quad (13)$$

where A is the stress optical coefficient, $\Delta\sigma$ is the difference in principal stresses normal to the path, and t is the plate thickness over the path coordinate z.

Preliminary observations were made to confirm the existence of a residual mouth-opening displacement at the median cracks. Vickers indentations on annealed soda-lime glass slabs were viewed parallel to both the surface and one of the impression diagonals (Fig. 1): optical paths displaced laterally about the indentation centre, and of depth comparable with that of the deformation zone, were accordingly investigated. The retardation was not measurably affected by the presence of the crack surfaces – the median crack normal to the optical path remained practically invisible in the birefringent image. The sign of the retardation was such that the principal stress along the surface normal always exceeded the principal stress along the surface tangent. Since the former stress component necessarily vanishes at the free surface, we conclude that the residual force on the median cracks, in order to accommodate the surrounding surface compression, must itself be tensile.

Quantitative information was obtained by viewing similar indentations normal to the glass surface. To relate this information to the requirements of geometrical similitude, namely that the spatial extent of the residual field scales with the impression half-diagonal a (Fig. 1), and the intensity of the field likewise with the hardness H,

where, by definition,

$$H = P^*/2a^2 \tag{14}$$

for Vickers indenters, Equation 13 may be more conveniently rewritten in the normalized form

$$\Gamma = (AH^{1/2}P^{*1/2}/2^{1/2}) \int_0^{t/a} [\Delta\sigma(z/a)/H]\, \mathrm{d}(z/a). \tag{15}$$

Then, if the retardation were always to be measured at the same relative position in the residual field, the integral quantity in Equation 15 should be invariant for any given indentation system.

Measurements of the optical retardation were accordingly made close to the impression sides, where maxima occurred, as a function of peak indentation load. (In this orientation, the principal stresses are, by symmetry, radially and tangentially directed.) Comparative tests were made on both annealed ($\sigma_s = 0$) and thermally tempered ($\sigma_s = -\sigma_R = -128$ MPa) glass surfaces, stress optical coefficient $A = 2.84\ \mathrm{TPa}^{-1}$, to investigate any possible effects of an imposed surface stress on the residual indentation field. Hardness values were measured directly from the impressions, in accordance with Equation 12, giving $H = (5.7 \pm 0.2)$ GPa (annealed) and $H = (5.5 \pm 0.2)$ GPa (tempered). The results are plotted as $\Gamma/AH^{1/2}P^{*1/2}$ versus P^* in Fig. 2. The constancy of the plot confirms the invariance of the integral quantity in Equation 15, thereby justifying the geometrical similarity principle for the glass studied here. Also, the fact that the data for annealed and tempered surfaces are indistinguishable within the scatter band demonstrates the insensitivity of the residual indentation field to extraneous forces. This last point is not surprising, in view of the high stress-concentrating power of sharp indenters – the relatively small surface stresses encountered in typical glass surfaces (cf. σ_R with H, above) are hardly likely to exert any significant influence on events within the irreversible deformation zone. Finally, noting that the threshold for median cracking was (3 ± 1) N for annealed glass and (10 ± 4) N for tempered glass, we may infer from Fig. 2 that the intensity of the residual field (as reflected in the integral component of Equation 15) is not significantly diminished by the onset of fracture: i.e. the effective centre load P_r remains constant as the median cracks extend. We may indeed conclude that χ_r in Equation 3 is constant for a given indenter–specimen system.

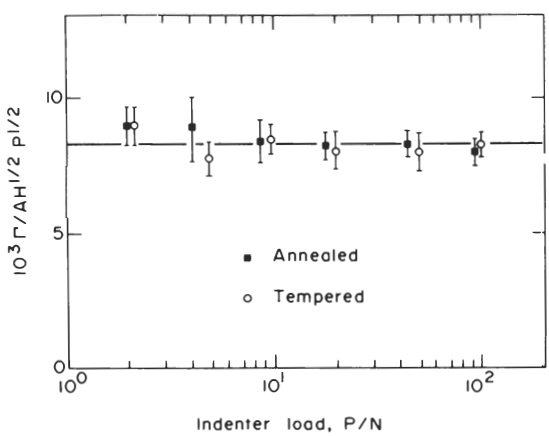

Figure 2 Bi-refringence data for residual Vickers impressions in annealed and tempered soda-lime glass. Bars on data points represent experimental measurement errors.

3.2. Median crack evolution

Observations of median crack response during the Vickers indentation cycle were made to investigate the predictions of Section 2. Two methods were used:

(i) Glass laths ≈ 50 mm × 6 mm × 3 mm (cut from glass discs – see Part 2) were indented *in situ* on the stage of an inverted microscope, and viewed from directly below the contact site in reflected polarized illumination. This set-up allowed the sideways extension of the median cracks to be followed directly. The indenter was mounted on a motor-driven double screw, which in turn acted against an instrumented proving ring to give a continuous record of the load delivered to the specimen [13]. The motor drive could be conveniently halted at any point during the contact for photographic purposes. A dry nitrogen enclosure about the specimen assembly provided an inert environment for equilibrium crack growth.

(ii) Similarly indented laths were broken in four-point bending, with the mutually orthogonal median cracks aligned normal and parallel to the tension axis. Failure initiated from the cracks in the normal orientation, which could then be examined by reflection microscopy. Crack arrest markings evident wherever the stress field suffered perturbations at halt points in the loading provided a pictorial record of fracture development.

Our first series of observations was taken with annealed laths indented on a rigid base support, i.e. with stress-free surfaces. Micrographs from a typical indentation sequence are shown in Figs. 3 and 4. We may note the symmetry of the patterns

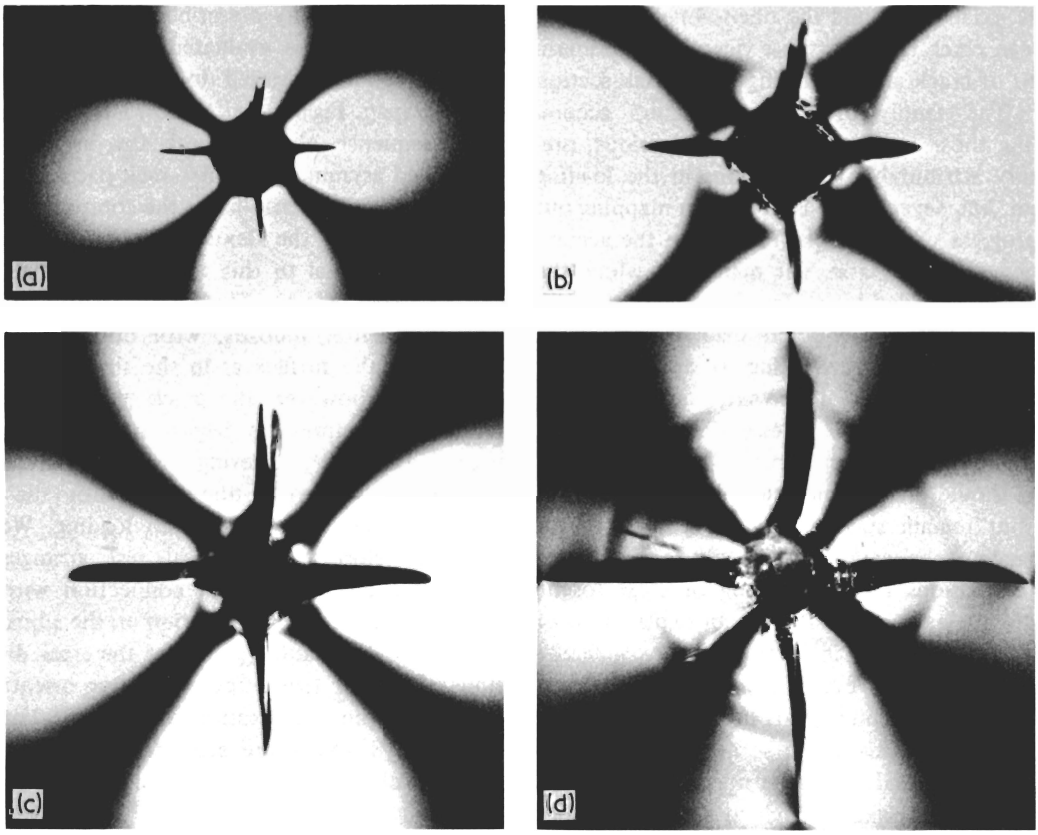

Figure 3 Median crack evolution in a stress free ($\sigma_s = 0$) surface of soda-lime glass, Vickers indenter. Axial views, at (a) partial load $P\uparrow = 47$ N, (b) maximum load $P^* = 90$ N, (c) partial unload $P\downarrow = 30$ N, (d) full unload $P\downarrow = 0$. (Lateral cracks also visible as faint Newton's ring system). Width of field 720 μm.

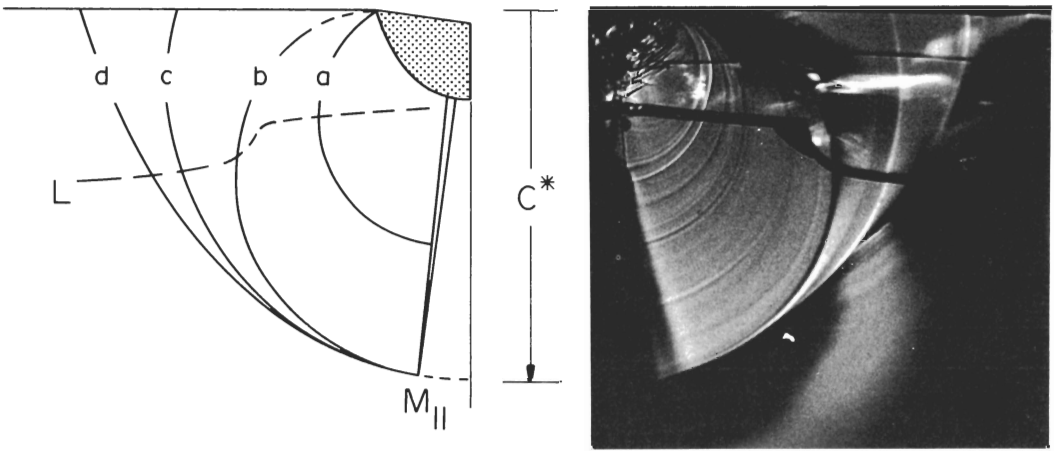

Figure 4 Half-side view of median crack shown with horizontal trace in Fig. 3 above, and half-schematic diagram mapping out growth fronts. Arrest positions marked correspond to (a), (b), (c), (d) in the axial views. Note absence of downward extension on unloading. $M_{||}$ denotes (slightly inclined) median crack parallel to compression axis. L denotes lateral crack. Width of half-field 650 μm.

in the axial views, and the one-to-one correlation between crack traces in these views and maximum widths of crack arrest markings in the half-section view. The family of fainter markings accompanying those labelled in Fig. 4 is spurious, presumably attributable to vibrations in the loading system, but nevertheless is helpful in mapping out the progress of the crack front, as in the accompanying half schematic. The manner in which the configuration develops from a "contained", sub-surface penny flaw at full loading to a surface half-penny at full unloading is apparent [4]. However, there is no downward crack extension during unloading. Thus the essential prediction for stress-free surfaces in Section 2, that median cracks should grow monotonically with increasing load but remain stationary with decreasing load (no healing), appears to apply only for characteristic dimensions measured along or close to the indentation axis. We shall offer an explanation of this kind of behaviour in Section 4.

The sequence of events depicted in Fig. 3 was observed for maximum loads in the range ≈ 20 to 150 N. Outside this range some variants in the evolution occurred: at higher maximum loads the median cracks broke through to the surface prior to unloading [3]; at lower maximum loads cracks did not even initiate until unloading commenced, in which case the surface half-penny geometry could be attained without passing through the contained-penny stage. However, regardless of the load region, the final shape was always reasonably close to that of the ideal half-penny.

Similar observations using the axial viewing apparatus were made on thermally tempered glass surfaces. (The tendency for tempered glass to shatter in a break test did not allow for a systematic study of section views of the median cracks.) Other than that the scale of the fracture was smaller, and higher maximum loads were needed to initiate the medians, the pattern of behaviour was as for stress-free surfaces. This is entirely in accord with the trends outlined for constant compression surfaces in Section 2.

Finally, a series of tests was run on laths supported on knife edges symmetrically disposed about the load axis, such that an uniaxial, load-dependent surface compression developed during the indentation. The Vickers pyramid was oriented to produce median cracks normal and parallel to the compressive stress, corresponding to surface states $\sigma_s = -\sigma_F^* P/P^*$ (Equation 5b) and $\sigma_s = 0$ respectively. For any prescribed load P^* the peak compression σ_F^*, as evaluated from simple beam theory, could be varied by adjustment of the support span. Figs. 5 and 6 show a typical indentation sequence obtained with this arrangement. A marked asymmetry in the crack pattern is now evident: the crack parallel to the compression axis is unaffected by the flexure (cf. Fig. 3), whereas the crack normal to this axis is substantially inhibited in its growth. The asymmetry diminishes as the indenter unloads, with both cracks extending to the surface as in the stress free specimen. Now, however, the crack experiencing the unloading compression begins to extend downward, ultimately achieving a depth somewhere intermediate between the values for the two orthogonal cracks at maximum loading. We are therefore close to the ideal test arrangement alluded to in Section 2 in connection with extracting quantitative information on the adjustable indentation constants χ_e and χ_r: the crack dimensions $c_\parallel^*$ and $c_\perp^\dagger$ (subscripts indicating orientation relative to the compression axis) appropriate to Equations 8 and 9 are accordingly indicated in the half-schematic of Fig. 6. Measurements from 10 well-developed crack systems formed at a peak load $P^* = 90$ N at $\sigma_F^* = 55$ and 110 MPa, two stress levels for which downward extension was observed during unloading of the minor median crack, gave $c_\parallel^* = (363 \pm 20)\,\mu$m and $c_\perp^\dagger = (214 \pm 18)\,\mu$m (see Fig. 7); together with $K_c = (0.75 \pm 0.05)$ MPa m$^{1/2}$ [14], Equations 8 and 9 yield $\chi_e = 0.032 \pm 0.008$ and $\chi_r = 0.026 \pm 0.003$ for soda-lime glass.

With the indentation parameters thus determined, and using a specially calibrated value $\Omega = 0.30$ for the geometrical constant pertinent to orthogonal half-penny cracks in a uniform surface stress field (Appendix), Equation 7 may be used to calculate the crack depth throughout the entire contact cycle for any given σ_s. Fig. 7 compares $P(c)$ functions computed in this way with experimental data from the indentation/flexure test series. The basic features of crack response predicted for flexural surfaces in Section 2.2 are apparent in this plot, although there is some systematic discrepancy in quantitative agreement: we may note, for instance, that some downward growth is observed during unloading at $\sigma_F^* = 55$ MPa, which compares with the critical quantity $(\sigma_F^*)_c = 65$ MPa calculated from Equation 12.

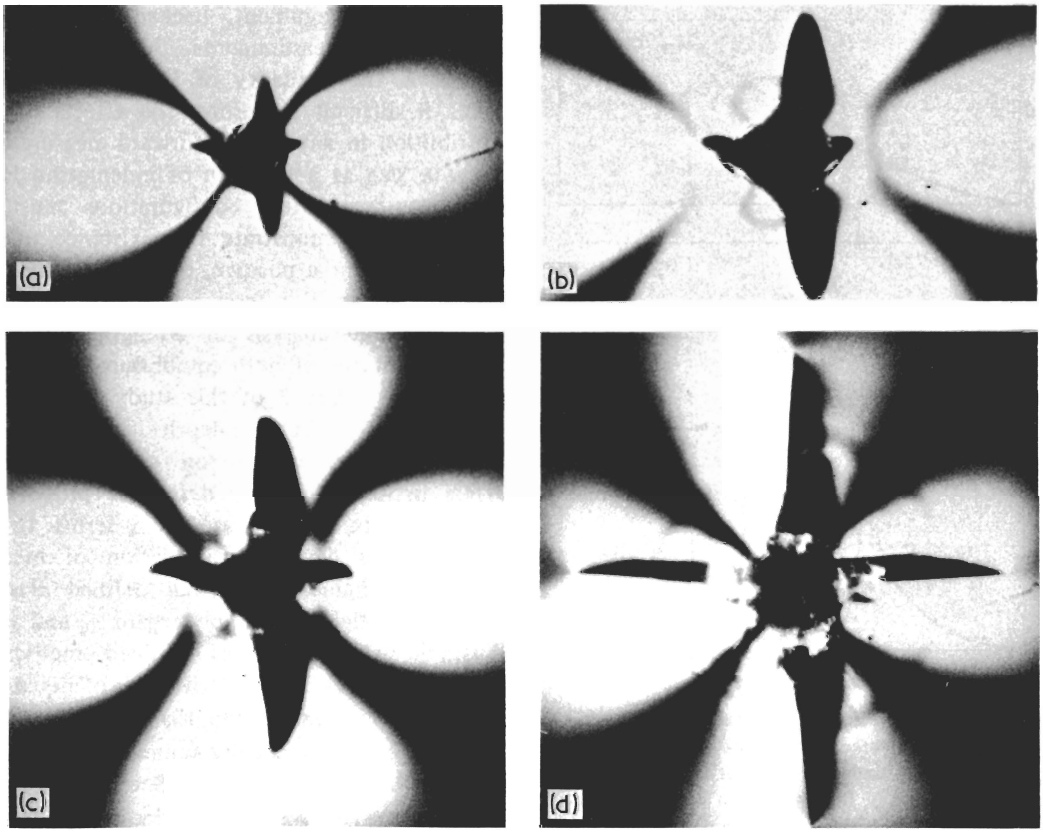

Figure 5 Median crack evolution of flexed ($\sigma_F^* = 110$ MPa) surface of soda-lime glass. Axial views at (a) partial load $P\uparrow = 52$ N, (b) maximum load $P^* = 90$ N, (c) partial unload $P\downarrow = 35$ N, (d) full unload $P\downarrow = 0$. Flexural compression acts normal to crack with horizontal trace. (Lateral cracks again faintly visible.) Width of field 720 μm.

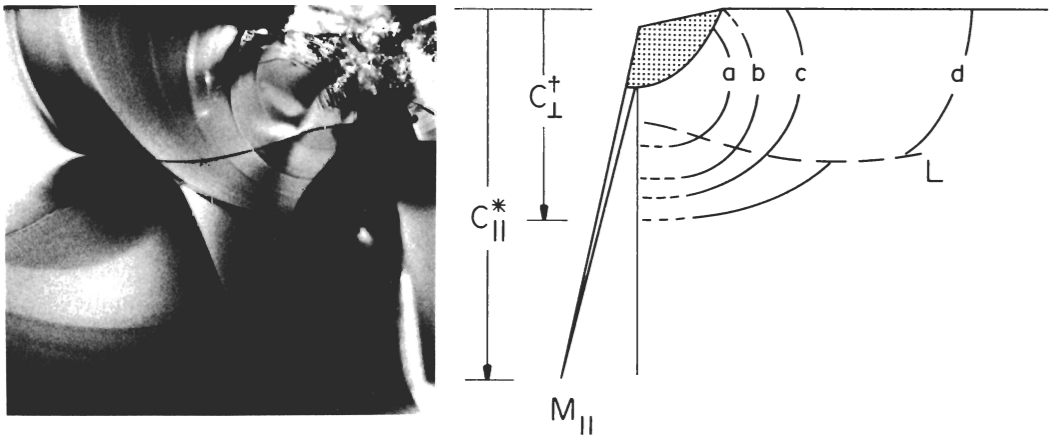

Figure 6 Half-side view of median crack shown with horizontal trace in Fig. 5 above, and half-schematic diagram mapping out growth fronts. Arrest positions marked correspond to (a), (b), (c), (d) in the axial views. Note downward extension on unloading (obscured partially by minor chipping). $M_{\parallel}$ denotes (slightly inclined) median crack parallel to compression axis. In this particular example, incidence of lateral crack L between stages (c) and (d) has prematurely obstructed downward extension. Width of half-field 650 μm.

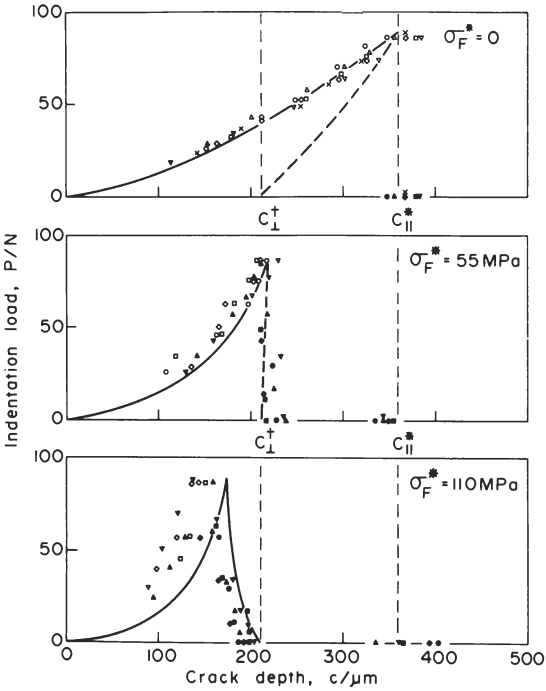

Figure 7 Fracture mechanics plot for median cracks in soda-lime glass subjected to various levels of flexural compression during indentation. Curves represent predictions of Equation 7, in conjunction with Equation 5b, using calibrated indentation constants (broken curves correspond to crack healing). Data points represent crack depth measurements from profile views. Each symbol represents different crack, with open symbols denoting loading half-cycle, closed symbols denoting unloading half-cycle.

At the conclusion of each indentation cycle it was noted that the final crack configuration could be maintained for more than 30 min in the dry nitrogen enclosure without significant expansion. However, immediately on opening the system to laboratory atmosphere, the cracks exhibited further, time dependent growth. The extent of this growth, as observed in the inverted microscope setup, was not inconsiderable, demonstrating the intensity of the residual field. Typically, after a 30 min exposure to air, the cracks had extended from 363 μm to 440 μm.*

4. Discussion

Our analysis of the contribution of residual elastic–plastic stresses to the driving force for median fracture in sharp contact derives from a simple scaling argument, backed up by stress bi-refringence measurements. As mentioned in Section 2, the similarity of Equations 2 and 3 makes it difficult to resolve the effects of this contribution in any straightforward measurement of crack size as a function of indentation load: certain surface stress configurations must be contrived to demonstrate the existence of the residual term in a positive, quantitative manner. Nevertheless, such a term has important implications in the analysis of strength properties, under conditions of both equilibrium and kinetic fracture [7]. Part 2 of this study will explore these implications in some depth.

Any treatment based on scaling principles suffers in its inability to determine proportionality constants, in this case the χ terms. In the absence of a detailed formulation of median fracture mechanics in a well defined elastic–plastic stress field, we simply regard χ_e and χ_r as adjustable parameters to be obtained empirically. Moreover, implicit in the derivations of Equations 2 and 3 is the assumption that the field which drives the cracks is radially symmetrical, whereas the observations described in Section 3.2 show clear evidence for a strong angular dependence in the fracture evolution; the relations derived in Section 2 are considered to apply only to the crack coordinate along the load axis. Some insight into the origin of this asymmetry may be gained by considering the nature of the long-range contact field through which the median cracks ultimately propagate, as represented by the Boussinesq point-load elasticity solution [3]. Fig. 8 shows that the distribution of the principal stress normal to the crack plane is indeed strongly angular dependent, but that one can subdivide this stress into symmetrical and asymmetrical components. The symmetrical component is tensile, and accordingly provides the elastic driving force implicit in the penny crack relation Equation 2. The asymmetrical component is compressive and surface confined – with the stress intensity in proportion to the contact load, this component acts in a manner somewhat analogous to that of a superposed compressive flexure field, thereby accounting for the inhibited expansion of the surface crack.

*Previous calibrations of the indentation constant $\chi(=\chi_e + \chi_r)$ for strength degradation analyses (e.g. see [6, 11] in Part 2 of this study) were carried out after exposures of such duration, and therefore do not correspond to strict equilibrium conditions.

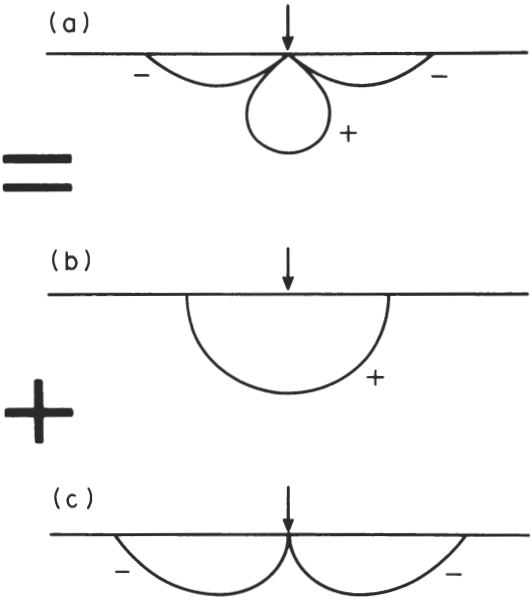

Figure 8 Polar plot of principal stresses normal to median plane in point-contact elastic field (a), showing subdivision into symmetrical (b) and asymmetrical (c) components.

There are also a number of other assumptions in the residual stress analysis which might be expected to contribute to discrepancies between theoretical prediction and observed behaviour; e.g. that negligible reversible plasticity occurs during indenter unloading and that the residual force term P_r remains constant during crack formation ("dead weight" crack loading). In addition, factors such as indenter geometry, and material inhomogeneity and anisotropy, would need to be considered in any complete treatment of the problem. The present simplistic formulation nevertheless serves usefully in accounting for the general features of crack evolution in sharp indenter fields, and, provided the adjustable indentation constants are calibrated under conditions appropriate to in-service environments, in establishing a basis for the prediction of contact-related fracture processes.

Appendix

The stress intensity factor for cracks of characteristic size c in a uniform tensile field σ is given by

$$K = \sigma(\pi\Omega c)^{1/2}, \qquad \text{(A1)}$$

i.e. of the same form as Equation 4. For an ideal full penny crack in an infinite medium the geometry term Ω is $4/\pi^2$ [8]. However, for the more complex configuration of Fig. 1 in which two mutually orthogonal half-penny cracks intersect the boundary of a semi-infinite medium along their diameters, Ω must be modified by free surface effects. In the absence of a theoretical fracture mechanics analysis of this configuration Ω is best determined by empirical calibration.

Some experimental strength data, taken on the same glass as used here, suffice for this purpose [15]. Test pieces in the form of discs nominally 50 mm in diameter and 3 mm in thickness were indented with a Vickers pyramid in the manner described in the text. The discs were then annealed to remove all traces of the residual stress field about the indentation (as verified by birefringence measurements). In case the annealing had blunted the crack tips the discs were then stressed subcritically in biaxial flexure in a moist environment, indented face on the tension side, until some slow crack growth was observed. The test environment was then changed to dry nitrogen, the surface traces of the median cracks measured, and the discs taken to failure. Results for 20 such tests in the strength range 35 to 70 MPa gave

$$\sigma c^{1/2} = (0.77 \pm 0.05)\ \text{MPa m}^{1/2} = K_c/(\pi\Omega)^{1/2}. \qquad \text{(A2)}$$

With $K_c = (0.75 \pm 0.05)\ \text{MPa m}^{1/2}$, Equations A1 and A2 combine to give $\Omega = 0.30 \pm 0.08$.

Acknowledgements

This work was supported by the Australian Research Grants Committee.

References

1. B. R. LAWN and T. R. WILSHAW, *J. Mater. Sci.* **10** (1975) 1049.
2. B. R. LAWN and D. B. MARSHALL, in "Fracture Mechanics of Ceramics", edited by R. C. Bradt, D. P. H. Hasselman and F. F. Lange (Plenum, New York, 1978) p. 205.
3. B. R. LAWN and M. V. SWAIN, *J. Mater Sci.* **10** (1975) 113.
4. B. R. LAWN and E. R. FULLER, *ibid.* **10** (1975) 2016.
5. J. J. PETROVIC, R. A. DIRKS, L. A. JACOBSON and M. G. MENDIRATTA, *J. Amer. Ceram. Soc.* **59** (1976) 177.
6. M. V. SWAIN, *J. Mater. Sci.* **11** (1976) 2345.
7. B. R. LAWN and D. B. MARSHALL, *J. Amer. Ceram. Soc.* **62** (1979) 106.
8. B. R. LAWN and T. R. WILSHAW, "Fracture of Brittle Solids" (Cambridge University Press, London, 1975) Chapter 3.
9. M. IMAOKA and I. YASUI, *J. Non-cryst. Solids* **22** (1976) 315.

10. C. M. PERROTT, *Wear* **45** (1977) 293.
11. R. HILL, "The Mathematical Theory of Plasticity" (Oxford University Press, London, 1950) Ch. 5.
12. A. J. MONACK and E. E. BEETON, *Glass Ind.* **20** (1939) 127, 185, 223, 257.
13. V. R. HOWES, *Glass Tech.* **15** (1974) 148.
14. S. M. WIEDERHORN, *J. Amer. Ceram. Soc.* **52** (1969) 99.
15. P. CHANTIKUL, B. R. LAWN and D. B. MARSHALL, *ibid.* (in press).

Received 5 December 1978 and accepted 15 January 1979.